

Using the $(3N)$ -Dimensional Generalized Lorenz Systems as a Testbed for Data Assimilation: The Ensemble Kalman Filter

SUNGJU MOON^a AND JONG-JIN BAIK^a

^a*School of Earth and Environmental Sciences, Seoul National University, Seoul, South Korea*

(Manuscript received 9 April 2021, in final form 25 July 2021)

ABSTRACT: The feasibility of using a $(3N)$ -dimensional generalization of the Lorenz system in testing a traditional implementation of the ensemble Kalman filter is explored through numerical experiments. The generalization extends the Lorenz system, known as the Lorenz '63 model, into a $(3N)$ -dimensional nonlinear system for any positive integer N . Because the extension involves inclusion of additional wavenumber modes, raising the dimension allows the system to resolve smaller-scale motions, a unique characteristic of the present generalization that can be relevant to real modeling scenarios. Model imperfections are simulated by assuming a high-dimensional generalized Lorenz system as the true system and a generalized system of dimension less than or equal to the dimension of the true system as the model system. Different scenarios relevant to data assimilation practices are simulated by varying the dimensional differences between the model and true systems, ensemble size, and observation frequency and accuracy. It is suggested that the present generalization of the Lorenz system is an interesting and flexible tool for evaluating the effectiveness of data assimilation methods and a meaningful addition to the portfolio of testbed systems that includes the Lorenz '63 and '96 models, especially considering its relationship with the Lorenz '63 model. The results presented in this study can serve as useful benchmarks for testing other data assimilation methods besides the ensemble Kalman filter.

KEYWORDS: Data assimilation; Kalman filters; Differential equations; Uncertainty; Numerical analysis/modeling; Nonlinear dynamics

1. Introduction

As operational numerical weather prediction (NWP) models began to take shape around the world, whether there exists a finite limit on atmospheric predictability has increasingly become a salient question both from the theoretical and practical points of view (Yoden 2007). Presciently, Thompson (1957) pointed out the uncertainties in the initial state as a possible cause of this hypothetical limit on atmospheric predictability. This view was further advanced with the discovery of deterministic chaos in the three-dimensional system of Lorenz (1963), in which even a very small perturbation can result in a large difference in the solutions. In NWP, such a perturbation can be introduced in the form of errors stemming from uncertainties in observations as well as imperfections of the model itself (Orrell et al. 2001; Privé and Errico 2013). Since the observation and model errors are unlikely to coincide, it becomes necessary to reconcile between the two conflicting objectives of closely following the observations and of adhering to the model's trajectory (Bröcker and Szendro 2012). The process of furnishing an analysis by appropriately combining observations and model outputs is called data assimilation.

The ensemble Kalman filter (EnKF) is a popular data assimilation method originally conceived as a stochastic alternative to the extended Kalman filter (EKF) for strongly nonlinear dynamics (Evensen 1994). Although the EnKF, unlike other more mature methods such as the four-dimensional

variational method (4DVar; Talagrand and Courtier 1987; Thépaut and Courtier 1991), has yet to be widely used operationally, its ease of implementation and competitive performance make the EnKF one of the most promising data assimilation methods available today (Kalnay 2003, 2010). The first real-world application was in oceanography. Evensen and Van Leeuwen (1996) used the EnKF to assimilate satellite altimeter data with a quasigeostrophic ocean model. In a comparison exercise against 4DVar, Lorenc (2003) recognized the potential of the EnKF for use in medium-range ensemble NWP systems but recommended a hybrid method using 4DVar to model the evolution within a short-time window and using the EnKF to model the evolution from one window to next. One particular concern was that the EnKF on high-resolution satellite data may require a very large ensemble. Promising early results in applications to atmospheric data assimilation were reported by Houtekamer et al. (2005) using real observation data and an operational global forecasting model.

Over the years, various modifications or extensions of the EnKF have been suggested in order to resolve some of the issues with the original formulation such as the problem of inbreeding (Houtekamer and Mitchell 1998; Van Leeuwen 1999) and the importance of treating observations as random variables (Burgers et al. 1998). Other such modifications include the ensemble adjustment Kalman filter (EAKF; Anderson 2001), the ensemble transform Kalman filter (ETKF; Bishop et al. 2001), the ensemble square root filter (EnSRF; Whitaker and Hamill 2002), and the local ensemble transform Kalman filter (LETKF; Hunt et al. 2007; Yang et al. 2012). Many of these developments were first presented alongside the test results using simplified systems of ordinary differential equations (ODEs),

Corresponding author: Jong-Jin Baik, jjbaik@snu.ac.kr

most notably, the three-dimensional system of Lorenz called the Lorenz '63 model (Lorenz 1963) and a more general system of arbitrary dimension known as the Lorenz '96 model (Lorenz 1996; Lorenz and Emanuel 1998; Lorenz 2006).

Since ensemble-based data assimilation methods are computationally expensive when implemented directly in a realistic model for the atmosphere, it is often advantageous to test new data assimilation methods, particularly the ones based on ensemble runs, on a smaller nonlinear model such as the Lorenz system. Evensen (1997) used the Lorenz '63 model to compare the performance of the EnKF with other data assimilation methods while varying the observation frequency. A similar comparison template was used by Pu and Hacker (2009), through which the EnKF was compared against various other related methods such as the EAKF, EnSRF, and ETKF while varying the ensemble size and the inflation factor for the background error covariance. Lei et al. (2012b) demonstrated the advantages of using a nudging–EnKF hybrid approach which allows for the seamless application of the EnKF via nudging-type terms computed from the flow-dependent, time-varying error covariance matrix. This approach was initially explored through numerical experiments using the Lorenz '63 model before the analysis was extended to the Weather Research and Forecasting (WRF) Model simulations (Lei et al. 2012a). Goodliff et al. (2015) used the Lorenz '63 model to test several hybrid approaches including that combining the 4DVar with the ETKF for its high nonlinearity and in order to avoid dealing with localization necessary in some higher-dimensional models (Anderson 2012; Bocquet and Farchi 2019). The Lorenz '63 and '96 models are often the first testbed choices for evaluating new particle filters as well, which are closely related to and can be thought of as generalizations of Kalman filtering (Elsheikh et al. 2013; Yeong et al. 2020). Besides testing new data assimilation methods, the Lorenz models historically have also served as ideal testing grounds for other ensemble-based tools including the nonlinear local Lyapunov vectors (Feng et al. 2014) and bred vectors (Zhang et al. 2015) as well as performance estimation tools such as the contextual formulation of model evidence (Carrassi et al. 2016).

In many aspects, the nonlinear ODE system known as the Lorenz '63 model is an ideal candidate for an initial testing of a data assimilation method. It is highly nonlinear yet simple enough, consisting of only three ODEs, so that the computation of numerical solutions does not require huge computational resources. It is relatively well-known and well-understood at least compared to other nonlinear models. There now exists an extensive literature on various properties of the Lorenz '63 model (Sparrow 1982; Tucker 1999; Osinga 2018) including self-synchronization (Afraimovich and Verichev 1986; Pecora and Carroll 1990). Moon et al. (2020) derived the $(3N)$ - and $(3N + 2)$ -dimensional generalization of the Lorenz '63 model for any positive integer N , building upon the extension method used by Shen (2014, 2015) and Moon et al. (2017). In this method, higher-dimensional systems are obtained by including additional higher wavenumber modes in the series expansions, which are to be truncated for the conversion of the governing partial differential equations (PDEs) to the ODEs comprising the resultant extension of the Lorenz system. Like the Lorenz '96 model, the

generalization of Moon et al. (2020) can set the dimension to be arbitrarily high; however, it should be noted that the Lorenz '96 model does not arise from any simplifications of governing equations (Herrera et al. 2011) nor is it a true high-dimensional counterpart of the Lorenz '63 model. The $(3N)$ - and $(3N + 2)$ -dimensional generalizations admit the three-dimensional Lorenz system as its lowest-dimensional member. Moreover, raising the dimension in this way bears a meaningful interpretation beyond simply furnishing a larger nonlinear system. Because raising the dimension following Moon et al. (2020) is tied to the inclusion of higher wavenumber modes in the derivation, the higher the dimension is, the finer scale of motions the system can resolve. Considering that one of the causes of a model's imperfection is that there is a limit to how small a scale it can resolve, it becomes a plausible testbed setup to have the true system take on a higher dimension than the model system. As an added benefit, the generalizations provide a way to quantify how different the model system is from the true system through the dimensional difference between the two systems. Given these advantages, it is desirable to include the $(3N)$ - and $(3N + 2)$ -dimensional generalizations into the portfolio of potential testbed choices for initial evaluation of new data assimilation methods alongside the Lorenz '63 and '96 models.

In this study, we test an implementation of the ensemble Kalman filter on the $(3N)$ -dimensional generalized Lorenz systems of Moon et al. (2020), simulating various scenarios by changing the ensemble size, model accuracy, and observation frequency and accuracy. There are three motivating questions behind conducting these simulations. First, how does the EnKF perform in the presence of highly nonlinear dynamics in a high-dimensional system compared to that in a low-dimensional system such as the Lorenz '63 model? Second, to what extent can the EnKF compensate for the difference between the true and model systems stemming from their dimensional difference? Third, how do the various factors affecting the EnKF performance interact with each other, including the model accuracy measured by the dimensional difference, and is there any generalizing trend in these interactions?

Section 2 introduces the $(3N)$ -dimensional system and provides basic information regarding the particular implementation of the EnKF used here. Section 3 presents the results of the numerical experiments by comparing the data assimilation performance of the EnKF under various conditions. Since the overarching framework adopted here should apply to all other ensemble-based data assimilation methods, these results can also serve as benchmarks for testing other data assimilation methods using the $(3N)$ -dimensional system in the future. Finally, a summary and conclusions are given in section 4.

2. Methodology

a. The $(3N)$ -dimensional generalized Lorenz system

Consider the governing PDEs for two-dimensional Rayleigh–Bénard convection in the x and z directions and the following series expansions for the streamfunction ψ and temperature perturbation θ (Moon et al. 2020):

$$\psi \approx \frac{1+a^2}{a} \sum_{n=1}^N \{X_n \sqrt{2} \sin(\pi ax) \sin[(2n-1)\pi z]\}, \quad (1)$$

$$\theta \approx \frac{\pi^3(1+a^2)^3}{a^2} \sum_{n=1}^N \{Y_n \sqrt{2} \cos(\pi ax) \sin[(2n-1)\pi z] \\ - Z_n \sin(2n\pi z)\}, \quad (2)$$

where $a = 1/\sqrt{2}$ is constant and N is a positive integer. It can be shown that the three-dimensional ODE system of Lorenz (1963) in variables X_1 , Y_1 , and Z_1 can be obtained by plugging in Eqs. (1) and (2) into the governing PDEs with $N = 1$. The $(3N)$ -dimensional system in variables $X_1, \dots, X_N, Y_1, \dots, Y_N$, and Z_1, \dots, Z_N can be derived in the same manner for any positive integer N .

The $(3N)$ -dimensional generalized Lorenz system of Moon et al. (2020) consists of the ODEs of the following form:

$$\dot{X}_k = -d_k \sigma X_k + \frac{\sigma}{d_k} Y_k, \quad (3)$$

$$\dot{Y}_k = r X_k - d_k Y_k + \sum_{(i,j) \in P_k} (j X_i Z_j \mathcal{S}_Y), \quad (4)$$

$$\dot{Z}_k = -k^2 b Z_k + \sum_{(i,j) \in Q_k} (k X_i Y_j \mathcal{S}_Z), \quad (5)$$

for all integer $k \leq N$. Here, $d_k \equiv [a^2 + (2k-1)^2]/(1+a^2)$. The parameters σ , r , and b are, respectively, the Prandtl number, the Rayleigh parameter, and the geometric parameter from the Lorenz system (Lorenz 1963). Consisting of the ordered pairs of integers, (i, j) , satisfying the conditions $i + j = k$, $j - i = k - 1$, or $i - j = k$ is the set P_k that determines which variables are multiplied together in Eq. (4). These terms, which are made up of products of two variables, are accompanied by a sign function \mathcal{S}_Y , which is -1 if the condition $j - i = k - 1$ is met and is otherwise $+1$. Similarly, the set Q_k for determining the nonlinear terms made up of products of two variables in Eq. (5) consists of the ordered pairs (i, j) satisfying the conditions $j + i = k + 1$, $i - j = k$, or $j - i = k$. The accompanying sign function for these nonlinear terms in Eq. (5) is \mathcal{S}_Z , which is $+1$ if the condition $j + i = k + 1$ is met and is otherwise -1 . Note that these nonlinear terms are not arbitrarily chosen but are the result of strictly following the derivation method of Lorenz (1963) and its extensions by Shen (2014). Periodicity diagrams in the dimension- r and dimension- σ spaces reveal that there exists a long stretch of chaotic solutions from dimension 3 to dimension 33 for the parameter choices of $r = 500$, $\sigma = 50$, and $b = 8/3$ (Moon et al. 2020), so we use these parameters for testbed simulations hereafter.

b. Implementation of the ensemble Kalman filter

Suppose our goal is to reproduce the solutions of a highly nonlinear system, such as one of the $(3N)$ -dimensional Lorenz systems, by assimilating sparsely distributed observations with the outputs of an imperfect model. We can consider the true solution in this setup to be the numerical solution of the given $(3N)$ -dimensional Lorenz system. We can then simulate having sparse observations by sampling the true solution with some observation error covariance matrix \mathbf{R} . At each observation time step, which is sparsely set by design, we can set \mathbf{d} to be the

n -dimensional vector, $n < 3N$, of the observations plus some observation error ε pulled from the n -dimensional normal distribution $\mathcal{N}(\mathbf{0}, \mathbf{R})$. In the implementation, the degree to which the overall observations are off is controlled by the observation error variance, and \mathbf{R} is formed as a diagonal matrix with the observation error variance as the diagonal entries. The square root of \mathbf{R} obtained from its eigen decomposition is multiplied by a random number drawn from the standard normal distribution to form the perturbation term added to the true solution at each observation time step. As a result, the observations will have random errors proportional to the observation error standard deviation (Burgers et al. 1998).

Ensembles of model trajectories can be formed by applying an artificial forcing to the model system. Following Evensen (2003), we progress the model state in variable ψ from the time step $k - 1$ to k with stochastic forcing by

$$\psi_k = \mathbf{f}(\psi_{k-1}) + \sqrt{\Delta t} \sigma \mathbf{q}_k, \quad (6)$$

where \mathbf{f} is the model system without forcing, Δt is the model time step size, σ is the standard deviation of the theorized model error, and ρ is an amplification parameter set as 50 in the implementation. The model error \mathbf{q} with variance 1 is assumed to be normally distributed and can be implemented using a random number generator. The background error covariance matrix should also be provided to initialize the imperfect model.

In a typical testbed setup such as that used in Pu and Hacker (2009), \mathbf{f} in Eq. (6) is given by the true system so that the true and model systems would be identical besides the forcing. With the $(3N)$ -dimensional generalization, we have in our toolbox the ability to generate two Lorenz systems differing in their dimensions. Higher-dimensional Lorenz systems are thought to resolve smaller-scale motions, and it can thus be said that they are closer to the governing PDEs for thermal convection than their lower-dimensional counterparts. Utilizing this feature, we can assign a high-dimensional system as the true system and a forced lower-dimensional system as the model system, mimicking the imperfections inherent to models due to limited knowledge about the real system or resolution available to the modeler. In this way, the framework has real conceptual relevance to modeling. It is easy to imagine a situation when the full governing system with a large number of variables is only partially known to the modeler who only has access to some lower-dimensional approximations of the reality. In this study, we focus on simulating this type of model imperfection stemming from it being assigned a system with the dimension lower than the dimension of the true system. Note that the current setup is reminiscent of the setup for checking chaos synchronization between two generalized Lorenz systems with different dimensions explored by Moon et al. (2021), wherein it was reported that the closer the two coupled systems are in terms of their dimensions, the more strongly they tend to synchronize.

Now, consider forming an ensemble of K members using the model. We would like to assimilate the observational data with the model outputs using the ensemble Kalman filter method. For each time step, the Kalman gain matrix \mathbf{K} is given by

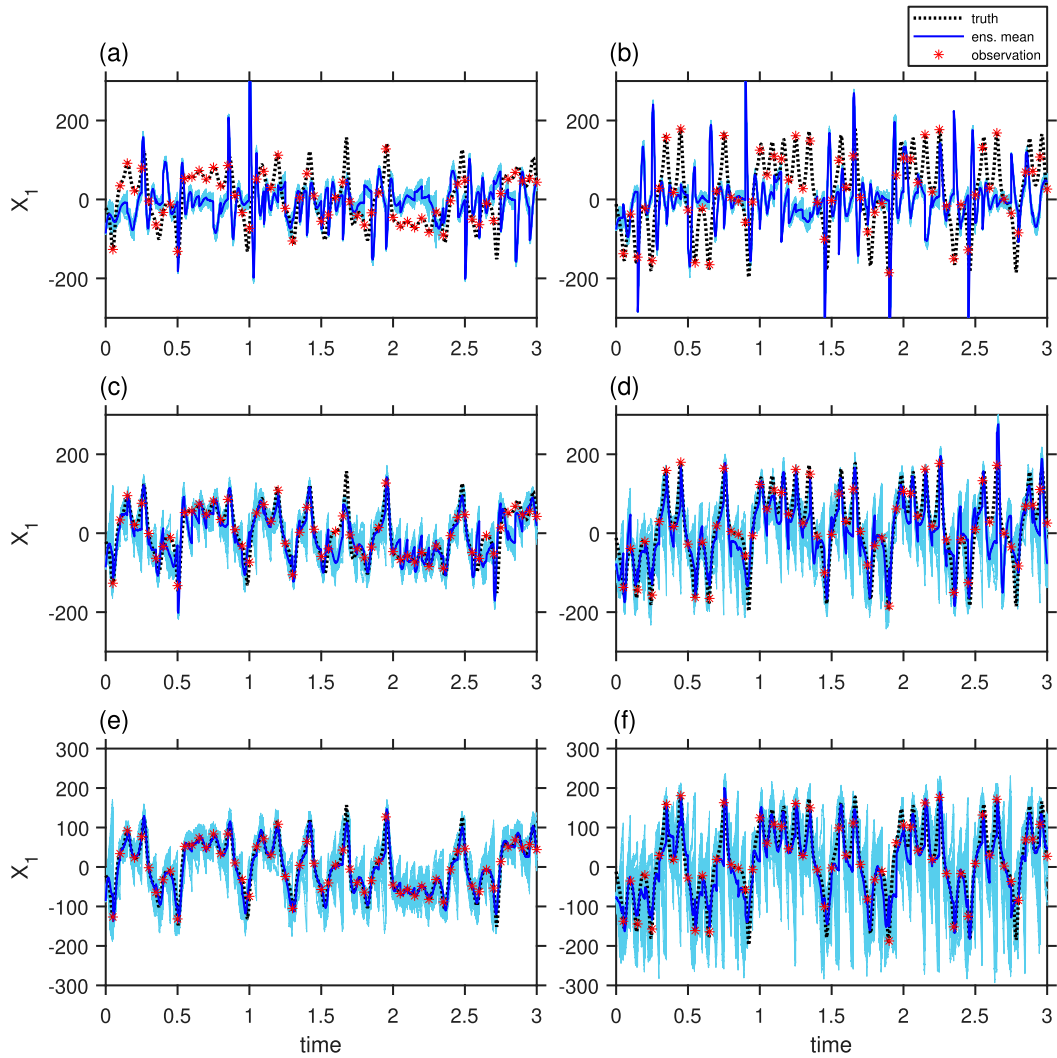


FIG. 1. Time series of the true solution (black dotted) along with observations (red asterisks) taken at every 500 time steps, 50 ensemble members (cyan solid) assimilated using observations and the model outputs, and the ensemble mean (blue solid) with the nine-dimensional Lorenz system as the true system and the (a) 3-, (c) 6-, and (d) 9-dimensional Lorenz systems given as the model systems and with the 30-dimensional Lorenz system as the true system and the (b) 3-, (d) 15-, and (f) 30-dimensional Lorenz systems given as the model systems.

$$\mathbf{K} = \mathbf{P}^f \mathbf{H}^T (\mathbf{R} + \mathbf{H} \mathbf{P}^f \mathbf{H}^T)^{-1}, \quad (7)$$

where \mathbf{P}^f is the (forecast) ensemble covariance matrix, \mathbf{H} is the linear observation operator, and the superscript T indicates the transpose operation (Evensen 2006). We use the identity observation operator for the simplified setup, which assumes that the observations are direct; that is, no conversions are required between observations and model states. For the general case, we can consider the (nonlinear) observation operator \mathcal{H} and let \mathbf{H} denote the linearized version of \mathcal{H} in a matrix form.

For computation of the Kalman gain matrix in Eq. (7), we use the following formulae (Evensen 1994; Houtekamer and Mitchell 1998):

$$\mathbf{P}^f \mathbf{H}^T = \frac{1}{K-1} \sum_{i=1}^K (\mathbf{x}_i^f - \overline{\mathbf{x}}^f) [\mathcal{H}(\mathbf{x}_i^f) - \overline{\mathcal{H}(\mathbf{x}^f)}]^T, \quad (8)$$

$$\mathbf{H} \mathbf{P}^f \mathbf{H}^T = \frac{1}{K-1} \sum_{i=1}^K [\mathcal{H}(\mathbf{x}_i^f) - \overline{\mathcal{H}(\mathbf{x}^f)}] [\mathcal{H}(\mathbf{x}_i^f) - \overline{\mathcal{H}(\mathbf{x}^f)}]^T, \quad (9)$$

where the overline indicates ensemble mean. Note that the inverse in the implementation is replaced with the Moore-Penrose pseudoinverse (Moore 1920; Penrose 1955) in case we encounter matrices that are singular or computationally expensive to invert (Evensen 2003).

Once we have the Kalman gain matrix \mathbf{K} , the analysis states $\{\mathbf{x}_i^a\}$ of the ensemble members can be updated by

$$\mathbf{x}_i^a = \mathbf{x}_i^f + \mathbf{K} [\mathbf{d} - \mathcal{H}(\mathbf{x}_i^f) + \varepsilon_i], \quad (10)$$

where ε_i is the observation error. We can repeat the above assimilation process at each observation time step, updating \mathbf{K} and incorporating new observations as they arise.

3. Results and discussion

a. Effects of ensemble size and model accuracy

Sample time series results are shown in Fig. 1 using two different true systems. In the left column, the true system's dimension (i.e., the true dimension) is set to be 9-dimensional and in the right column, the 30-dimensional system is chosen as the true system. The model dimensions are gradually raised going from top to bottom (3-, 6-, and 9-dimensional on the left; 3-, 15-, and 30-dimensional on the right). Similar to Evensen (1997), the initial conditions for the true system are given by $X_i = 1.5$, $Y_i = -1.5$, and $Z_i = 25.5$ for all $i = 1, 2, \dots, N$ in the $(3N)$ -dimensional systems, but it should be noted that any choice of initial conditions is expected to yield similar results so long as it belongs to the same basin of attraction. The numerical integrations are done using the fourth-order Runge–Kutta method with $\Delta t = 10^{-4}$. The initial spinup time of 1 time unit is given prior to $t = 0$ (i.e., $t = 0$ is when the spinup is over), and the integration is performed for 3 additional time units from $t = 0$ to $t = 3$.

The observations are taken at every 500 time steps with the error variance of 1. Due to the small observation error variance, these evenly spaced out observations thus appear to be fairly consistent with the true solution (Figs. 1a,b). How the observation error variance affects the assimilation results will be discussed in section 3b. Each ensemble consists of 50 imperfect model members generated with uniformly distributed random forcing with amplification magnitude $\rho = 50$ following Eq. (6), and the initial guess for the forecast error is set randomly up to magnitude 50. At each observation time step, the ensemble members are updated using the Kalman gain matrix \mathbf{K} , and the updated ensemble member states are then averaged to obtain the analysis mean. The differences in the initial conditions combined with the random forcing produce a nicely spread out ensemble of assimilated member states with the analysis mean trajectory at the center.

Notice how in both 9- and 30-dimensional cases, the closer the model's dimension is to the true dimension, the closer also are the assimilated solutions to the true solutions. The ensemble means noticeably deviate from the true solution in Figs. 1a,b where the dimensional differences are the greatest. Already in Figs. 1c,d, the time series for the true solution and ensemble mean are in agreement with one another except for the occasional misalignments around $t \in [1.5, 2]$ in Fig. 1c and around $t \in [2.5, 3]$ in Fig. 1d. In Figs. 1e,f, the model systems and the true systems have the same dimensions, and thus their solutions show better alignment with one another than in the other cases.

The results in Fig. 1 are obtained using the identity observation operator. A nonidentity observation operator can lead to a more realistic setup since in operational systems there is often found a nonlinear relationship between a model variable and observations. Like nonlinearity in the forecast

model, nonlinearity in the observation operator can render a Kalman filter-based data assimilation algorithm suboptimal due to the underlying assumption in the Kalman filter theory (Tong and Xue 2005). Figure 2 shows sample time series results using the following nonidentity observation operator defined similarly to Hamilton et al. (2019) but with an amplification factor:

$$\mathcal{H}(\mathbf{x}) = \mathcal{H} \begin{pmatrix} \vdots \\ X_k \\ Y_k \\ Z_k \\ \vdots \end{pmatrix} = \begin{pmatrix} \vdots \\ \rho \sin(X_k) \\ Y_k - \rho \\ \rho \cos Z_k \\ \vdots \end{pmatrix} \quad (11)$$

for $k = 1, \dots, N$. As in Fig. 1, the analysis mean is closer to the true trajectory when the model system's dimension is closer to the true system's dimension. The results using the three-dimensional model system (Figs. 2a,b) seem less refined compared to the rest, and it is possible that certain combinations of true and model dimensions lead to stability issues in our current setup. The effects of having a nonidentity observation operator would also depend on the choice of function. As such, in the subsequent analysis, we focus on the simplest setup in which the identity observation operator is used.

To quantify how different the assimilated guesses are from the true solutions, the root-mean-square (rms) errors are computed as a function of ensemble size or time and are shown in Fig. 3. Given time t , the rms error E_t is computed by

$$E_t = \sqrt{\frac{1}{3} \sum_{j=1}^3 \left(\frac{1}{K} \sum_{i=1}^K V_{j,i} - V_{j,\text{tr}} \right)^2}, \quad (12)$$

where K is the ensemble size, $V_{j,i}$ is the assimilated solution for the j th variable in the i th ensemble member, and $V_{j,\text{tr}}$ is the true solution for the j th variable. The variables used for the computations are chosen so that V_j corresponds to the solutions to X_1 , Y_1 , or Z_1 . These three variables are chosen because they are the shared variables across the systems even as dimension is varied.

The rms errors are then averaged over the last time unit of assimilation (i.e., from 2 to 3) and are plotted in Figs. 3a,b as a function of ensemble size. There is an inversely proportional relationship between the ensemble size and the time-averaged rms errors, but the effects of increasing the ensemble size already seems to be nearing saturation as early as 10–20 members. When the ensemble size is relatively small (≤ 10), data assimilation is not as effective, and the ensemble size affects the average rms error as strongly as the model's dimension does. When the ensemble size is large enough (≥ 20) on the other hand, it becomes clear that the closer the model's dimension is to the true dimension, the smaller the errors become. Such a relationship between the dimensional difference and rms errors can also be found in the time series of the rms errors. Figures 3c,d show the time series of the rms errors for the particular case where 50-member ensembles are used. The three-dimensional model almost consistently scores the

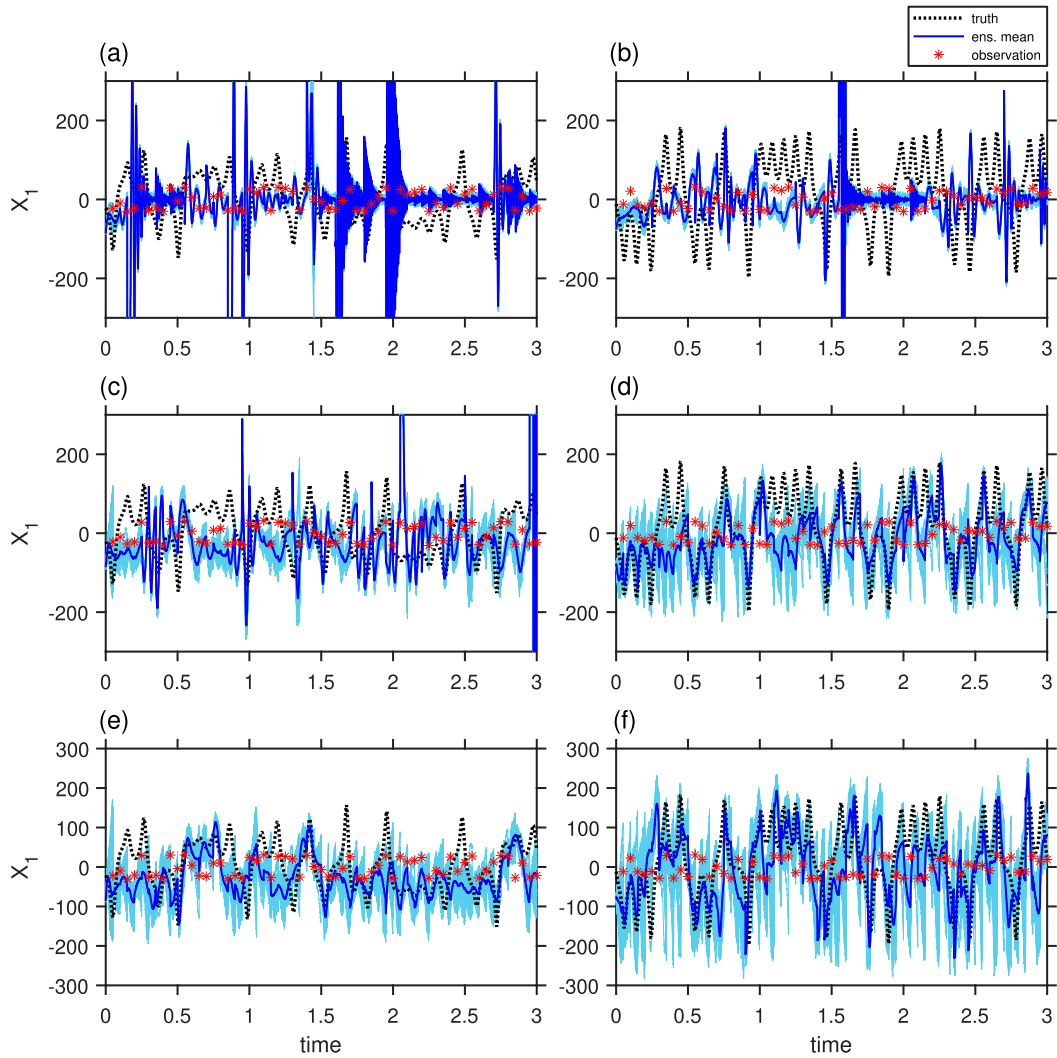


FIG. 2. As in Fig. 1, but using the nonidentity observation operator defined by Eq. (11).

largest rms error throughout the simulation time in both cases, which can be attributed to the large dimensional differences between the true and model systems. When the 30-dimensional system is given as the true system, the 15-dimensional model system already shows fairly small rms errors, comparable to the 30-dimensional model system for some time ($t \in [0, 1]$ in Fig. 3d), but it appears that the model system having the same dimension as the true system still performs better overall than when the model's dimension is lower.

It also appears that, if all other main drivers of errors are kept consistent, bringing the model system as close to the true system as possible in the first place can lead to huge leaps in reducing the rms error, more so than increasing the number of ensemble members. Figures 3a,b reveal that, at least for these systems, there is a limit to how much increasing the ensemble size alone can do to improve the data assimilation performance. A similar slowing-down of the effects of increasing the ensemble size beyond ~ 20 members is also reported in Pu and Hacker (2009). Note that in real systems where ensemble size

cannot keep up with observations, rank-deficiency problem is an issue (Houtekamer and Mitchell 2001) and increasing the ensemble size can have a crucial impact on mitigating this issue. After the effects of increasing the ensemble size saturate, the performance is mainly determined by the dimensional difference between the true and model systems. In practice, such an improvement of a model can come from, for example, the identification of an additional state variable or a previously unknown relationship between important state variables that can explain certain features of a smaller scale than what is resolvable by the currently available model. If the model involves a truncation, then reducing the severity of the truncation or refining the resolution of the model can also bring it closer to the true system as is the case in the $(3N)$ -dimensional generalization of the Lorenz system.

The robustness of these relationships, between ensemble size, model dimension, and the data assimilation performance of the EnKF, is examined with additional numerical experiments

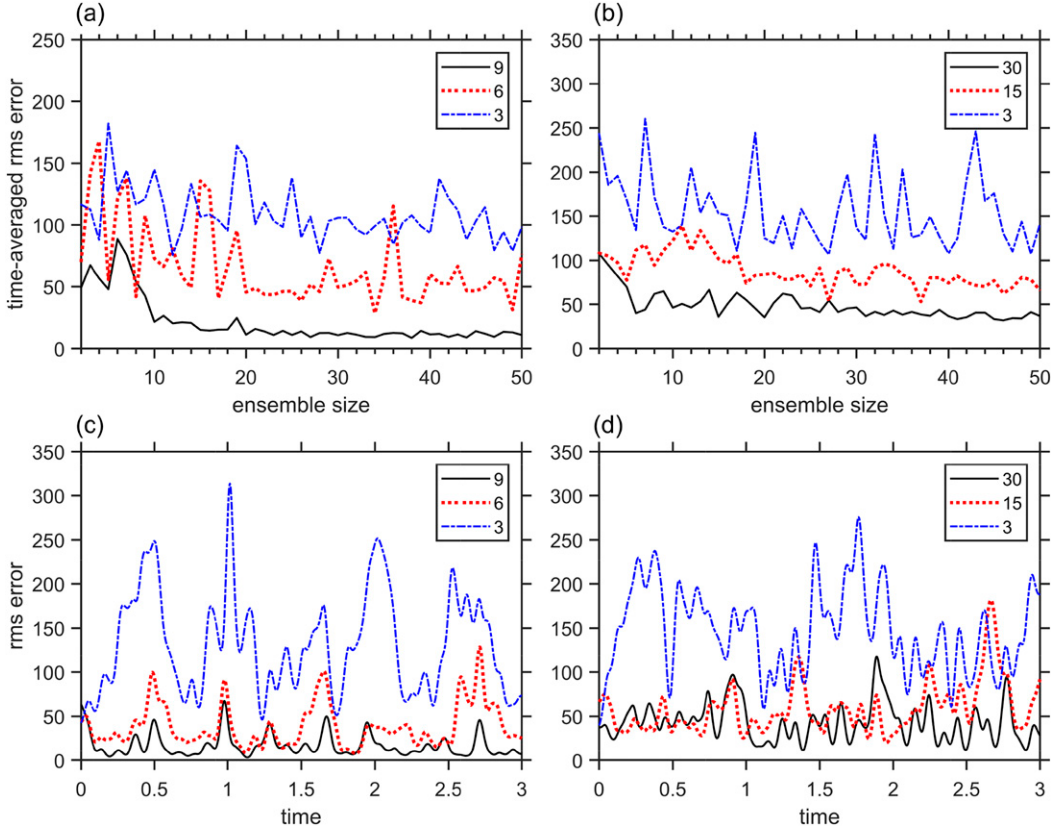


FIG. 3. (top) Root-mean-square (rms) errors averaged over time $t \in [2, 3]$ as a function of ensemble size (a) between the true solution from the 9-dimensional system and the assimilated ensemble mean using the 3-, 6-, and 9-dimensional systems (blue dash-dotted, red dotted, and black solid, respectively) as model systems and (b) between the true solution from the 30-dimensional system and the ensemble mean using the 3-, 15-, and 30-dimensional systems (blue dash-dotted, red dotted, and black solid, respectively) as model systems. (bottom) Time series of the rms errors between the true solutions and the assimilated ensemble means computed with 50 ensemble members for the cases (c) with the true solution from the 9-dimensional system and (d) with the true solution from the 30-dimensional system.

involving different ensemble sizes and a range of model dimensions. Figure 4 shows the results of further experiments performed across the model dimensions ranging from 3 to 30 with 5-, 50-, and 100-member ensembles, given the 30-dimensional Lorenz system as the true system. The overall inversely proportional relationship between the ensemble size and the time-averaged rms error is mostly consistent across the model dimensions. With the exception of model dimension 3 and, by a much smaller margin, model dimension 15, the time-averaged rms error decreases going from 5-member ensembles to 50-member ensembles. Likewise, except for model dimensions 18 and 21—by a tiny margin for model dimension 18—the time-averaged rms error decreases going from 50-member ensembles to 100-member ensembles.

With few exceptions, such as going from the model dimension 3 to 6 with 5-member ensembles, there is an overall inversely proportional relationship between the model dimension and the time-averaged rms error. This pattern becomes more robust when the ensemble size is larger. While the time-averaged rms error increases with the model dimension on four occasions in

the 5-member ensemble cases by wide margins in some cases, it occurs only twice for the 50-member ensemble cases including the increase going from model dimension 21 to 24. No such increase is seen in the 100-member ensemble cases. It is likely that the simulations with such a small ensemble size of 5 suffer from undersampling issues.

Figure 5 shows that this inversely proportional relationship is not limited to having the 30-dimensional system as the true system. Here, using 100-member ensembles, true dimensions ranging from 9 to 33 are tested for this hypothesized inversely proportional relationship between the model dimension and the time-averaged rms errors. The behavior of the implemented EnKF shown in Fig. 5 again confirms that the closer the model is to the true system in terms of their dimensions, the higher the accuracy of the predictions can be afforded by the data assimilation scheme. Interestingly, with the 100-member ensemble, the exceptional local uptick in the time-averaged rms error does not occur with the 6-dimensional model system like in Fig. 4 but with the 12-dimensional model system. The cases when the true system has 24 and 15 dimensions

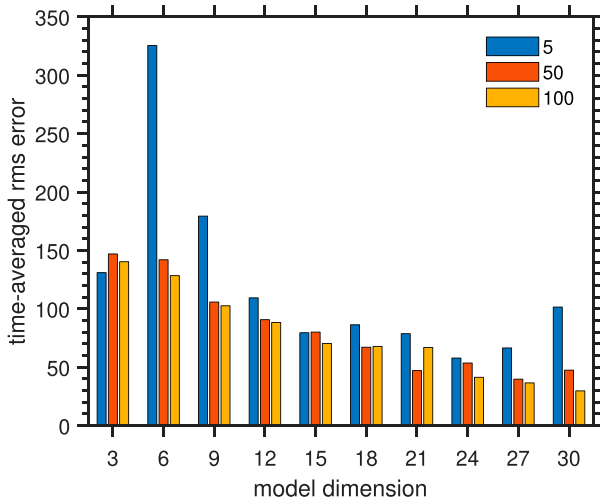


FIG. 4. Time-averaged rms errors between the true solution from the 30-dimensional system and the ensemble mean of the model solutions obtained from the $(3N)$ -dimensional systems with $N = 1, 2, \dots, 10$ assimilated using 5, 50, and 100 ensemble members.

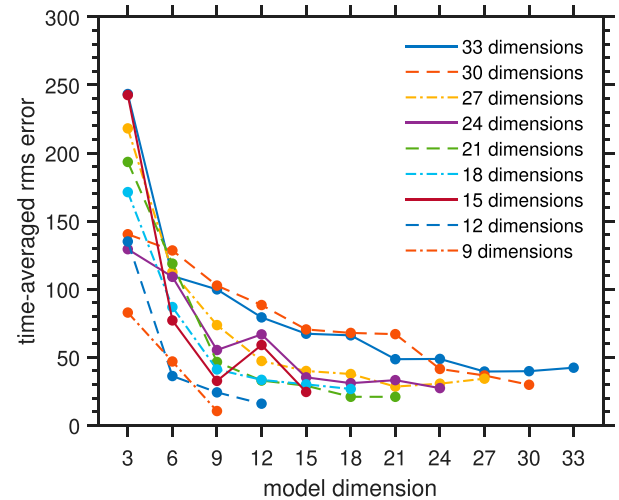


FIG. 5. Time-averaged rms errors between the true solutions from the $(3N)$ -dimensional system, $N = 3, 4, \dots, 11$, and the ensemble mean of the model solutions obtained from the $(3M)$ -dimensional systems with $M = 1, 2, \dots, N$ assimilated using 100 ensemble members.

show brief upticks in the time-averaged rms error at model dimension 12, going against the overall trend. This suggests that the uptick at model dimension 6 observed in the 5-member ensemble case shown in Fig. 4 does not reflect the overall trend but is merely an exceptional case given the particular simulation setup used here.

To ascertain the plausibility of our claims about these exceptional cases, we have rerun the experiments with model dimensions 9, 12, and 15 for true dimensions 15, 24, and 30 under a diversity of conditions as well as further computing the rms errors averaged over a longer period of time, that is, over the last 8 time units in experiments with 9 time units of assimilation time. The results are summarized in Tables 1 and 2, respectively. When averaged over the longer period of time, the rms errors tend to decrease with respect to the model dimension in more cases (indicated by bold letters in the tables) compared to when the averaging was done only over the last time unit, indicating that some of the exceptional rises in rms errors with respect to the model dimension seen in Table 1 were affected perhaps by only temporarily anomalous trends that were washed out by the longer-term averaging done for Table 2.

The stubborn cases that are still resistant to the monotonically decreasing trend in Table 2 can largely be broken up into two groups: first, when the model dimensions being compared are relatively close to one another and, second, when the ensemble size is small. Given the true dimension of 15, both the 9- and 12-dimensional models are fairly close to the true system and, therefore, can still perform adequately as models compared to, say, when the true dimension is much higher. Indeed, hardly any trend in rms errors can be found if only the tail ends (e.g., the three highest model dimensions) of the plots in Fig. 5 are compared.

As discussed earlier regarding Figs. 3a,b and 4, 5-member ensembles can be inadequate for drawing robust conclusions.

Note that the numbers in Table 1 are slightly different from the numbers used to plot Figs. 4 and 5 because certain randomness is involved with model perturbation in each run, and results using 5-member ensembles do show greater variability than those using larger ensembles. One of the most dramatic cases in point is the time-averaged rms error for the nine-dimensional system using a 5-member ensemble, which was computed to be 179.4 for Fig. 4 but is 142.8 in Table 1 from the reruns. For this particular case, five additional runs with different random seeds were arranged and their bootstrap distributions were calculated by resampling the rms errors 10 000 times, and this was repeated for the case using 100-member ensembles. When 5-member ensembles were used, the bootstrap distribution had the standard deviation of 10.32, much larger than 1.57 for when 100-member ensembles were used.

Last, raising the observation frequency seems to also influence how the time-averaged rms errors respond to raising the model dimension. Accordingly, section 3b investigates the effects of observation frequency and accuracy in greater detail.

b. Effects of observation frequency and accuracy

The observation error variance has so far been set as 1, which corresponds to the observations being sampled with impeccable accuracy considering the much larger magnitudes of the numerical solutions. Observations were taken at every 500 time steps with $\Delta t = 10^{-4}$, which corresponds to 60 data points within the simulation period of 3 time units. This is roughly equivalent to sampling observations at every 6 h over the course of a two week-long period in terms of observation frequency. As can be seen in Fig. 1, this distribution provides enough information for the models to perform reasonably well without the asterisk scatters appearing too sparse or too dense in the time series.

If the observation error variance can be kept at such a low level, it is reasonable to assume that having more frequent

TABLE 1. The rms errors computed for additional experiments under various conditions with the 15-, 24-, and 30-dimensional systems as the true systems and the 9-, 12-, and 15-dimensional systems as the model systems. The rms errors are averaged over the last time unit out of the three time units of total assimilation time. The bold font indicates that the rms error decreases monotonically with the model dimension.

Observation frequency	Ensemble size	True dimension									
		15			24			30			
		Model dimension			Model dimension			Model dimension			
9	12	15	9	12	15	9	12	15	9	12	15
50	5	51.8	56.9	59.1	35.8	47.0	51.2	46.9	64.9	73.5	
	50	20.6	32.1	10.1	14.5	29.6	18.4	28.2	34.4	20.5	
	100	8.8	27.4	35.5	25.4	32.4	15.1	34.7	19.2	16.0	
	200	42.7	33.8	16.5	19.8	31.4	17.7	23.9	20.5	19.3	
500	5	84.2	51.7	80.2	163.8	91.0	53.7	118.7	117.6	111.2	
	50	29.9	43.8	38.4	88.0	54.0	38.1	98.2	90.7	80.1	
	100	29.5	59.0	24.5	67.2	66.8	35.2	110.5	88.3	70.4	
	200	31.1	46.7	24.1	72.9	67.5	31.2	103.3	96.2	72.6	
1000	5	99.1	69.7	70.3	98.9	97.7	90.7	175.5	94.6	84.1	
	50	51.5	63.5	54.2	57.2	55.0	54.1	75.1	61.7	67.1	
	100	68.9	63.0	55.4	58.6	54.3	47.6	68.6	64.7	59.2	
	200	60.2	54.5	55.4	63.4	54.2	51.4	70.7	64.3	58.6	

observations will only lead to better predictions. It can become problematic, however, in situations when such high accuracies in observations are not guaranteed. Too frequent observations with low accuracy may steer the analysis away from the true trajectory in favor of the many inaccurate observation data points. In such situations, it becomes important to strike a balance between having too frequent observations and having too sparse observations based on the current knowledge about the expected accuracy of observations.

Figure 6 shows the trajectories for three demonstrative cases differing in the observation frequency and error variance. Note that the choppiness in the trajectories of Fig. 6a, more noticeable for the first few assimilation time steps, is due to the

intermittent approach of the EnKF. This issue was the target of the nudging–EnKF hybrid approach proposed by Lei et al. (2012b). The high-accuracy–high-frequency case with the observations taken at every 200 time steps with the error variance of 1 in Fig. 6a shows close alignment between the trajectories of the true solution and the ensemble mean of the model solutions. When the observation frequency is lowered with the same observation error variance, the alignment between the true and model solutions is not as good. Much of the outer parts of the true solution’s trajectory in Fig. 6b is not covered by the analysis trajectory. The trajectories for the assimilated individual member solutions are more spread out in Fig. 6b than in Fig. 6a, meaning that there are greater disagreements

TABLE 2. As in Table 1, but the rms errors are averaged over the last eight time units out of nine time units of total assimilation time. The bold font indicates that the rms error decreases monotonically with the model dimension.

Observation frequency	Ensemble size	True dimension									
		15			24			30			
		Model dimension			Model dimension			Model dimension			
9	12	15	9	12	15	9	12	15	9	12	15
50	5	27.8	31.7	44.2	59.3	63.6	70.5	59.2	66.4	85.1	
	50	28.5	23.4	8.2	31.3	42.2	21.5	32.0	53.9	22.8	
	100	15.5	15.0	16.2	42.9	39.5	18.0	48.1	33.0	22.5	
	200	11.0	35.6	8.1	33.6	19.2	15.5	30.8	27.8	20.1	
500	5	123.2	56.1	51.6	118.7	84.9	83.7	137.5	107.8	80.5	
	50	38.2	24.7	19.3	97.3	53.9	42.8	100.2	82.4	56.7	
	100	36.8	24.0	21.1	84.9	52.7	40.0	95.5	78.8	56.4	
	200	34.5	23.4	19.2	82.7	47.2	36.3	97.0	75.8	48.7	
1000	5	94.1	66.4	67.5	108.1	89.5	75.9	103.1	88.6	86.0	
	50	57.6	46.3	47.1	77.6	67.4	62.3	74.3	71.8	63.0	
	100	55.7	47.0	48.0	78.7	66.0	57.9	71.5	66.4	61.5	
	200	54.4	43.9	48.2	76.8	60.7	57.1	71.2	67.2	63.2	

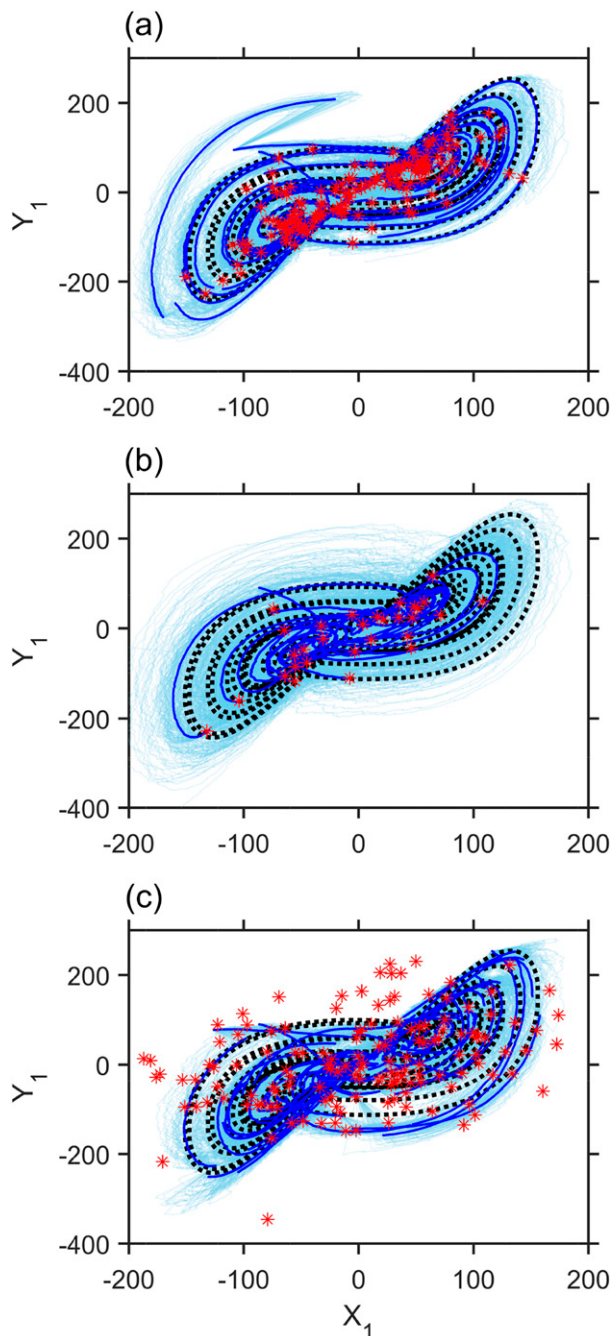


FIG. 6. Solution trajectories of the true solution (black dotted), assimilated ensemble members (cyan solid), and the ensemble mean (blue solid) along with observations (red asterisks) projected on the X_1 - Y_1 plane for the case when the observations are made (a) every 200 time steps with the error variance 1, (b) every 1000 time steps with the error variance 1, and (c) every 200 time steps with the error variance 5000. The ensemble size of 50 members is used for all cases. Both the true and model systems are given by the nine-dimensional Lorenz system.

among individual members when the observation frequency is lowered.

In Fig. 6c, observations are set to be less accurate with the error variance raised to 5000. As a result, the asterisk scatters in Fig. 6c representing the observations tend to be positioned way off the true solution's trajectory. The ensemble mean in Fig. 6c still shows decent agreement with the true solution at least from the angle of view shown here. Note that although 5000 is a fairly high error variance for the observations to have, this number can be reasonable in the context of the trajectory ranging from about -300 to 300 in the Y_1 direction and about -150 to 150 in the X_1 direction. In the Lorenz system and its extensions, the solution magnitudes are determined mainly by the parameter choices, especially the Rayleigh parameter r , and so the solution magnitudes should remain comparable regardless of the dimension of the system as long as the parameters are chosen consistently. Upon closer inspection, it can be seen that the ensemble mean in Fig. 6c still deviates farther away from the true solution's trajectory compared to the high-frequency-high-accuracy case shown in Fig. 6a.

The time-averaged rms errors computed over $t \in [2, 3]$ using Eq. (12) are plotted in Fig. 7 as a function of the square root of the observation error variance under various conditions for observation frequency and dimensions of the true and model systems being used. The model systems have the same dimension as the true systems in Figs. 7a and 7c corresponding to the 9- and 30-dimensional generalized Lorenz systems, respectively. Three different observation frequencies are considered, namely, every 200, 600, and 1000 time steps. In both Figs. 7a and 7c, the high observation frequency cases with observations taken at every 200 time steps initially have the smallest time-averaged rms errors among the three when the observation error variance is relatively low. Eventually, as the observation error variance is increased, the time-averaged rms errors for these cases rise to the highest value among the peers. When the inaccuracies in the observation is combined with further inaccuracies in the models, with the model systems having lower dimensions than the true systems as in Figs. 7b,d, the high-frequency cases show large time-averaged rms errors even when the observation error variance is low. It is the balanced case that tends to perform best overall as exemplified by the case with observations taken at every 600 time steps. Corresponding to each level of expected observation errors, therefore, there seems to exist an optimal observation frequency that provides just enough information without flooding the data assimilation processes with misleading observation errors.

It is suspected that the existence of the “sweet-spot” observation frequency has to do with the routinely adopted practices of *covariance inflation* and *localization*, which are not implemented in the present study. Covariance inflation is used to combat the “filter divergence problem” (Anderson and Anderson 1999) caused by the loss of variance through sampling errors. Localization deals with spurious sample correlations between observations and state variables. In EnKF systems, this is typically done by taking a Schur product between the covariance matrix \mathbf{P}^f and a correlation function, which is defined based on the distance between observations

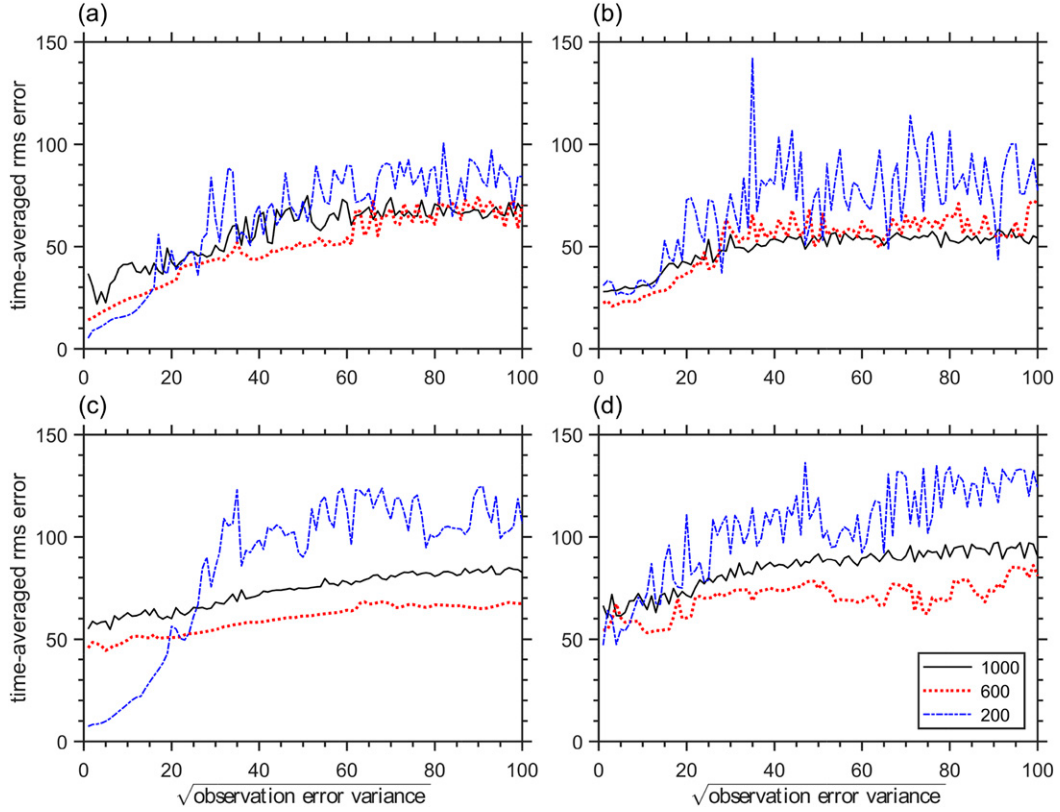


FIG. 7. Time-averaged rms errors between the true trajectory and the assimilated ensemble mean with a 50-member ensemble using observations made at every 200 (blue dash-dotted), 600 (red dotted), and 1000 (black solid) time steps as a function of the square root of observation error variance for the case with (a) the 9-dimensional system as both the true and model systems, (b) the 9-dimensional system as the true system and the 6-dimensional system as the model system, (c) the 30-dimensional system as both the true and model systems, and (d) the 30-dimensional system as the true system and the 15-dimensional system as the model system.

and state variables (Houtekamer and Mitchell 2001; Hamill et al. 2001). It has been pointed out that this so-called observation-space localization can make the EnKF less competitive in some cases compared to 4DVar, which does localization in the model space (Shlyraeva et al. 2019). Furthermore, for implementation in the generalized Lorenz systems, there may not be a clearly defined notion of distance since the variables reside in a dimensionless space. It might be possible to develop some notion of physical distance based on the interpretation of these systems as physical models for thermal convection; for example, Park et al. (2021) reconstructs flow and temperature patterns in Rayleigh–Bénard convection based on the numerically obtained chaotic attractors of an extended Lorenz system so that the results can be systematically compared against direct numerical simulation (DNS) results. At any rate, there exist several different approaches and tuning strategies for both covariance inflation and localization with varying success (Hamill and Whitaker 2005; Li et al. 2009; Anderson 2007), and we expect to further explore these more advanced implementations of the EnKF for the generalized Lorenz systems in a future study.

Note that even at fairly high observation error variances, the time-averaged rms errors plotted in Fig. 7 do not appear to be

particularly large in comparison with those in Fig. 4 or 5. In fact, Fig. 7 shows that the time-averaged rms errors even at very large observation errors are comparable to or smaller than those obtained with the 50-member cases at the lower end of the model dimension in Fig. 4 (model dimension 3, 6, and 9 having the rms error > 100), reiterating again the importance of having an accurate model to begin with for the data assimilation scheme to perform well. Given the seemingly high impact of assigning the models with lower-dimensional Lorenz systems on the rms errors, Fig. 8 provides a more systematic presentation regarding the effect of observation error and frequency by averaging the rms errors over all available lower-dimensional models for the 30-dimensional true system. In Fig. 8a, the average for the high-frequency cases (every 200 time steps) initially hits the smallest average rms errors among the three before eventually surpassing the others at high enough observation error variances (its square root ≥ 30), similar to the pattern seen in Fig. 7. The average for the cases with a medium level of observation frequency (every 600 time steps) beats the other cases (every 200 and 1000 time steps) in terms of data assimilation performance overall, particularly at moderately low observation error variances (its square root between ~ 20 and ~ 50).

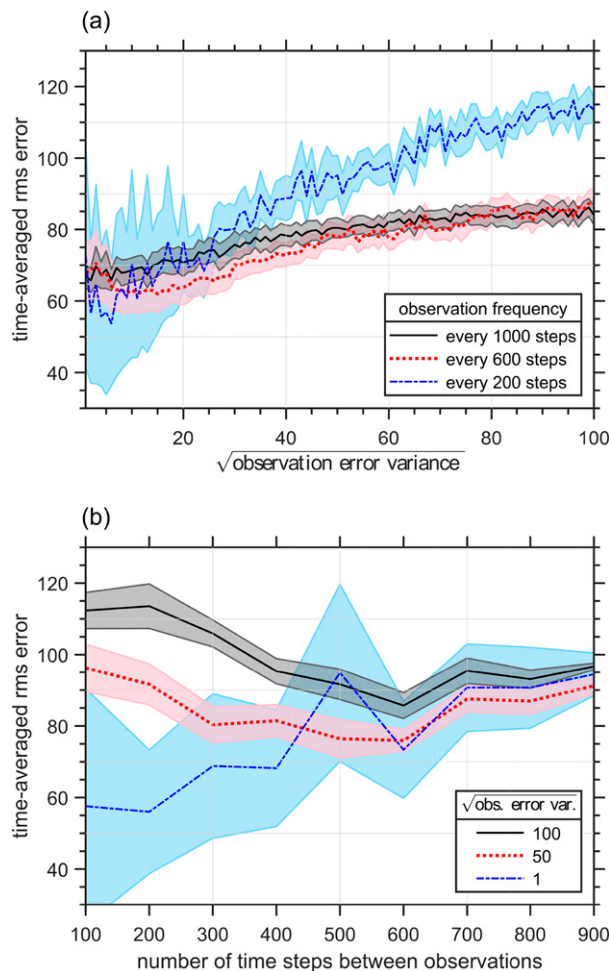


FIG. 8. Time-averaged rms errors averaged over all ($3N$)-dimensional model systems, $N = 1, 2, \dots, 10$, (a) as a function of the square root of observation error variance using observations made at every 200 (blue dash-dotted), 600 (red dotted), and 1000 (black solid) time steps and (b) as a function of observation frequency (the number of time steps from one observation time step to next) using observations with the square root of observation error variance 1 (blue dash-dotted), 50 (red dotted), and 100 (black solid). The root-mean-square errors are computed between the 30-dimensional true system's solutions and the 50-member ensemble mean of the updated model solutions.

In Fig. 8b, this observation frequency-dependence is further investigated for specific observation error variances (their square roots being 1, 50, and 100). As expected, the time-averaged rms error is not monotonic with respect to the level of observation frequency, although it tends to increase with sparser observations in the case when observations are highly accurate (observation error variance = 1). In the cases where observations are less accurate, the time-averaged rms errors gradually rise as the observation frequency increases from every 300 time steps to every 100 time steps. Although it is hard to make out clearly defined rms error-minimization points based on the graphs, the time-averaged rms errors for the cases

with relatively high observation error variances (their square roots being 50 and 100) appear to slowly rise back up as observations get sparser than the rate at every 600 time steps.

Notice the relatively spread out confidence intervals accompanying the high-frequency case in Fig. 8a in comparison with those for the other two cases, especially when the observation error variance is low (its square root ≤ 20). This high-sensitivity of the time-averaged rms errors when the observations are highly accurate is also noticeable in Fig. 8b. When individually inspected, it was found that the large time-averaged rms errors at these relatively low observation error variances have mostly originated from the cases with relatively low model dimensions. On the one hand, this may be an indication that, given highly accurate observations, the data assimilation performance reacts more sensitively to the model inaccuracies and their impact on the synchronization between the Lorenz systems rather than to small changes in observation-related variables. To maintain the performance stability against observation errors and, therefore, fairer evaluation of a given data assimilation method, one might need to impose a certain threshold on observation accuracy such as a lower bound for its square root at ~ 20 .

On the other hand, taken at face value, these results also suggest that if the model itself is highly inaccurate to begin with, then regardless of how frequent the observations are, they cannot save the data assimilation performance even with a very small error variance. Frequent observations can even amplify the existing discrepancies between the true and model trajectories in some cases by frequently invoking the highly inaccurate model results at each observation time step. Now, despite the relatively wide confidence intervals, the average for the high observation frequency cases does not solidly rise above the other two cases until the observation error variance is higher (its square root ≥ 30) at which point the confidence intervals become narrower. It can thus be inferred that the soaring average rms error for the high observation frequency cases, for the most part, is driven by the amplification of observation errors rather than that of model inaccuracies.

4. Summary and conclusions

The conditions for all of the main numerical experiments carried out in this study are summarized in Table 3. While the specifics of the experimental results presented here necessarily depend on the fine tuning of the simulation setup as well as on the data assimilation method being used, some general conclusions can still be drawn from these simulation results. It was observed that adopting a more accurately formulated model system can be more rewarding than increasing only the ensemble size or the observation accuracy or frequency. The need to address the delicate issue of choosing an optimal observation frequency by considering the expected level of observation error is also discussed, especially in connection with the need for implementing covariance inflation and localization.

Simulations with a large ensemble size show a clearly downward trend in the rms errors as the model dimension is raised. Since the same trend is also observed regarding chaos synchronization (Moon et al. 2021), it is speculated that the two

TABLE 3. Summary of the experimental conditions including the true and model dimensions, ensemble size, observation frequency and error variance, type of observation operator used, and observation and model biases along with the corresponding figure numbers. In all cases, the Lorenz equation parameters are given as $r = 500$, $\sigma = 50$, and $b = 8/3$ with initial conditions $(X_i, Y_i, Z_i) = (1.5, -1.5, 25.5)$, $i = 1, \dots, N$.

Experiment	True (model) dimension	Ensemble size	Observation frequency ^a (error variance)	Observation operator	Fig.
Sample time series	9 (3, 6, 9), 30 (3, 15, 30)	50	500 (1)	Identity Nonidentity	Fig. 1 Fig. 2
Ensemble size and model dimension experiments	9 (3, 6, 9), 30 (3, 15, 30) 30 (3, ..., 30) 9–33 (3, ...) ^b	2–50 5, 50, 100 100	500 (1)	Identity	Fig. 3 Fig. 4 Fig. 5
Observation accuracy and frequency experiments	9 (9) 9 (6, 9), 30 (15, 30) 3–30 (3, ...) ^b	50	200 (1), 1000 (1), 200 (5000) 200, 600, 1000 (1–10 000) 200, 600, 1000 (1–10 000), 100–900 (1, 50, 10 000)	Identity	Fig. 6 Fig. 7 Fig. 8

^a In terms of the number of time steps between observations.

^b All $(3N)$ -dimensional systems with dimension \leq true dimension.

phenomena are closely related and are caused by some inherent characteristics of the particular class of nonlinear dynamical systems of [Moon et al. \(2020\)](#). The apparent connections between data assimilation and generalized synchronization discussed in [Moon et al. \(2021\)](#) can also provide an interesting avenue for discovery especially because synchronization between true and model systems via observations can be thought of as an underlying framework for conceptual understanding of data assimilation ([Yang et al. 2006](#)).

It is beneficial to have the option of choosing among a variety of testbed models for testing a data assimilation method, as different models will come with their unique features and considerations. Unlike the Lorenz '96 model, raising the dimension in the $(3N)$ -dimensional generalization corresponds to considering additional Fourier modes in the governing equations out of which the ODE systems are obtained. This unique feature of the $(3N)$ -dimensional systems makes them an interesting choice of a model for testing data assimilation methods. In particular, because the $(3N)$ -dimensional generalization encompasses the Lorenz '63 model, more consistent comparisons between high- and low-dimensional cases can be made using this generalization together with the Lorenz '63 model.

It must be emphasized that different forcing magnitudes or model setups can change the outcome of the numerical experiments presented here. Caution must be practiced, therefore, when interpreting or drawing conclusions based on the results of simulations using simplified models such as the Lorenz system in a testbed setup. It would be worthwhile to investigate whether some of the broader conclusions drawn here are also found in testbed results using different formulations of the ensemble Kalman filter or other data assimilation methods, provided that consistent benchmark conditions are enforced.

Acknowledgments. The authors thank the editor and two anonymous reviewers for their helpful comments and detailed feedback. SM would also like to thank Dr. Seoleun Shin and

Dr. Alison Fowler for helpful discussions during the early stage of this research. This work was supported by the Small Grant for Exploratory Research (SGER) program through the National Research Foundation (NRF) of Korea (2018R1D1A1A02086007).

Data availability statement. Data generated and analyzed during the current study are available from the corresponding author upon request.

REFERENCES

- Afraimovich, V. S., and N. N. Verichev, 1986: Stochastic synchronization of oscillation in dissipative systems. *Radiophys. Quantum Electron.*, **29**, 795–803, <https://doi.org/10.1007/BF01034476>.
- Anderson, J. L., 2001: An ensemble adjustment Kalman filter for data assimilation. *Mon. Wea. Rev.*, **129**, 2884–2903, [https://doi.org/10.1175/1520-0493\(2001\)129<2884:AEAKFF>2.0.CO;2](https://doi.org/10.1175/1520-0493(2001)129<2884:AEAKFF>2.0.CO;2).
- , 2007: Exploring the need for localization in ensemble data assimilation using a hierarchical ensemble filter. *Physica D*, **230**, 99–111, <https://doi.org/10.1016/j.physd.2006.02.011>.
- , 2012: Localization and sampling error correction in ensemble Kalman filter data assimilation. *Mon. Wea. Rev.*, **140**, 2359–2371, <https://doi.org/10.1175/MWR-D-11-00013.1>.
- , and S. L. Anderson, 1999: A Monte Carlo implementation of the nonlinear filtering problem to produce ensemble assimilations and forecasts. *Mon. Wea. Rev.*, **127**, 2741–2758, [https://doi.org/10.1175/1520-0493\(1999\)127<2741:AMCIOT>2.0.CO;2](https://doi.org/10.1175/1520-0493(1999)127<2741:AMCIOT>2.0.CO;2).
- Bishop, C. H., B. J. Etherton, and S. J. Majumdar, 2001: Adaptive sampling with the ensemble transform Kalman filter. Part I: Theoretical aspects. *Mon. Wea. Rev.*, **129**, 420–436, [https://doi.org/10.1175/1520-0493\(2001\)129<0420:ASWTET>2.0.CO;2](https://doi.org/10.1175/1520-0493(2001)129<0420:ASWTET>2.0.CO;2).
- Bocquet, M., and A. Farchi, 2019: On the consistency of the local ensemble square root Kalman filter perturbation update. *Tellus*, **71A**, 1613142, <https://doi.org/10.1080/16000870.2019.1613142>.
- Bröcker, J., and I. G. Szendro, 2012: Sensitivity and out-of-sample error in continuous time data assimilation. *Quart. J. Roy. Meteor. Soc.*, **138**, 785–801, <https://doi.org/10.1002/qj.940>.
- Burgers, G., P. J. Van Leeuwen, and G. Evensen, 1998: Analysis scheme in the ensemble Kalman filter. *Mon. Wea. Rev.*, **126**,

- 1719–1724, [https://doi.org/10.1175/1520-0493\(1998\)126<1719:ASITEK>2.0.CO;2](https://doi.org/10.1175/1520-0493(1998)126<1719:ASITEK>2.0.CO;2).
- Carrassi, A., M. Bocquet, A. Hannart, and M. Ghil, 2016: Estimating model evidence using data assimilation. *Quart. J. Roy. Meteor. Soc.*, **143**, 866–880, <https://doi.org/10.1002/qj.2972>.
- Elsheikh, A. H., I. Hoteit, and M. F. Wheeler, 2013: A nested sampling particle filter for nonlinear data assimilation. *Quart. J. Roy. Meteor. Soc.*, **140**, 1640–1653, <https://doi.org/10.1002/qj.2245>.
- Evensen, G., 1994: Sequential data assimilation with a nonlinear quasi-geostrophic model using Monte Carlo methods to forecast error statistics. *J. Geophys. Res.*, **99**, 143–162, <https://doi.org/10.1029/94JC00572>.
- , 1997: Advanced data assimilation for strongly nonlinear dynamics. *Mon. Wea. Rev.*, **125**, 1342–1354, [https://doi.org/10.1175/1520-0493\(1997\)125<1342:ADAFSN>2.0.CO;2](https://doi.org/10.1175/1520-0493(1997)125<1342:ADAFSN>2.0.CO;2).
- , 2003: The ensemble Kalman filter: Theoretical formulation and practical implementation. *Ocean Dyn.*, **53**, 343–367, <https://doi.org/10.1007/s10236-003-0036-9>.
- , 2006: *Data Assimilation: The Ensemble Kalman Filter*. Springer, 330 pp.
- , and P. J. Van Leeuwen, 1996: Assimilation of Geosat altimeter data for the Agulhas Current using the ensemble Kalman filter with a quasigeostrophic model. *Mon. Wea. Rev.*, **124**, 85–96, [https://doi.org/10.1175/1520-0493\(1996\)124<0085:AOGADF>2.0.CO;2](https://doi.org/10.1175/1520-0493(1996)124<0085:AOGADF>2.0.CO;2).
- Feng, J., R. Ding, D. Liu, and J. Li, 2014: The application of nonlinear local Lyapunov vectors to ensemble predictions in Lorenz systems. *J. Atmos. Sci.*, **71**, 3554–3567, <https://doi.org/10.1175/JAS-D-13-0270.1>.
- Goodliff, M., J. Amezcuia, and P. J. Van Leeuwen, 2015: Comparing hybrid data assimilation methods on the Lorenz 1963 model with increasing non-linearity. *Tellus*, **67A**, 26928, <https://doi.org/10.3402/tellusa.v67.26928>.
- Hamill, T. M., and J. S. Whitaker, 2005: Accounting for the error due to unresolved scales in ensemble data assimilation: A comparison of different approaches. *Mon. Wea. Rev.*, **133**, 3132–3147, <https://doi.org/10.1175/MWR3020.1>.
- , —, and C. Snyder, 2001: Distance-dependent filtering of background error covariance estimates in an ensemble Kalman filter. *Mon. Wea. Rev.*, **129**, 2776–2790, [https://doi.org/10.1175/1520-0493\(2001\)129<2776:DDFOBE>2.0.CO;2](https://doi.org/10.1175/1520-0493(2001)129<2776:DDFOBE>2.0.CO;2).
- Hamilton, F., T. Berry, and T. Sauer, 2019: Correcting observation model error in data assimilation. *Chaos*, **29**, 053102, <https://doi.org/10.1063/1.5087151>.
- Herrera, S., D. Pazó, J. Fernández, and M. A. Rodríguez, 2011: The role of large-scale spatial patterns in the chaotic amplification of perturbations in a Lorenz'96 model. *Tellus*, **63A**, 978–990, <https://doi.org/10.1111/j.1600-0870.2011.00545.x>.
- Houtekamer, P. L., and H. L. Mitchell, 1998: Data assimilation using an ensemble Kalman filter technique. *Mon. Wea. Rev.*, **126**, 796–811, [https://doi.org/10.1175/1520-0493\(1998\)126<0796:DAUAEK>2.0.CO;2](https://doi.org/10.1175/1520-0493(1998)126<0796:DAUAEK>2.0.CO;2).
- , —, 2001: A sequential ensemble Kalman filter for atmospheric data assimilation. *Mon. Wea. Rev.*, **129**, 123–137, [https://doi.org/10.1175/1520-0493\(2001\)129<0123:ASEKFF>2.0.CO;2](https://doi.org/10.1175/1520-0493(2001)129<0123:ASEKFF>2.0.CO;2).
- , —, G. Pellerin, M. Buehner, M. Charron, L. Spacek, and B. Hansen, 2005: Atmospheric data assimilation with an ensemble Kalman filter: Results with real observations. *Mon. Wea. Rev.*, **133**, 604–620, <https://doi.org/10.1175/MWR-2864.1>.
- Hunt, B. R., E. J. Kostelich, and I. Szunyogh, 2007: Efficient data assimilation for spatiotemporal chaos: A local ensemble transform Kalman filter. *Physica D*, **230**, 112–126, <https://doi.org/10.1016/j.physd.2006.11.008>.
- Kalnay, E., 2003: *Atmospheric Modeling, Data Assimilation and Predictability*. 1st ed. Cambridge University Press, 341 pp.
- , 2010: Ensemble Kalman filter: Current status and potential. *Data Assimilation*, W. Lahoz, B. Khattatov, and R. Menard, Eds., Springer-Verlag, 69–92.
- Lei, L., D. R. Stauffer, and A. Deng, 2012a: A hybrid nudging-ensemble Kalman filter approach to data assimilation in WRF/DART. *Quart. J. Roy. Meteor. Soc.*, **138**, 2066–2078, <https://doi.org/10.1002/qj.1939>.
- , —, S. E. Haupt, and G. S. Young, 2012b: A hybrid nudging-ensemble Kalman filter approach to data assimilation. Part I: Application in the Lorenz system. *Tellus*, **64A**, 18484, <https://doi.org/10.3402/tellusa.v64i0.18484>.
- Li, H., E. Kalnay, and T. Miyoshi, 2009: Simultaneous estimation of covariance inflation and observation errors within an ensemble Kalman filter. *Quart. J. Roy. Meteor. Soc.*, **135**, 523–533, <https://doi.org/10.1002/qj.371>.
- Lorenc, A. C., 2003: The potential of the ensemble Kalman filter for NWP—A comparison with 4D-Var. *Quart. J. Roy. Meteor. Soc.*, **129**, 3183–3203, <https://doi.org/10.1256/qj.02.132>.
- Lorenz, E. N., 1963: Deterministic nonperiodic flow. *J. Atmos. Sci.*, **20**, 130–141, [https://doi.org/10.1175/1520-0469\(1963\)020<0130:DNF>2.0.CO;2](https://doi.org/10.1175/1520-0469(1963)020<0130:DNF>2.0.CO;2).
- , 1996: Predictability—A problem partly solved. *Proc. ECMWF Seminar on Predictability*, Vol. 1, Reading, United Kingdom, ECMWF, 1–18.
- , 2006: Predictability—A problem partly solved. *Predictability of Weather and Climate*, T. Palmer and R. Hagedorn, Eds., Cambridge University Press, 40–58.
- , and K. A. Emanuel, 1998: Optimal sites for supplementary weather observations: Simulation with a small model. *J. Atmos. Sci.*, **55**, 399–414, [https://doi.org/10.1175/1520-0469\(1998\)055<0399:OSFSWO>2.0.CO;2](https://doi.org/10.1175/1520-0469(1998)055<0399:OSFSWO>2.0.CO;2).
- Moon, S., B.-S. Han, J. Park, J. M. Seo, and J.-J. Baik, 2017: Periodicity and chaos of high-order Lorenz systems. *Int. J. Bifurcation Chaos*, **27**, 1750176, <https://doi.org/10.1142/S0218127417501760>.
- , J. M. Seo, and J.-J. Baik, 2020: High-dimensional generalizations of the Lorenz system and implications for predictability. *Phys. Scripta*, **95**, 085209, <https://doi.org/10.1088/1402-4896/ab9d3e>.
- , J.-J. Baik, and J. M. Seo, 2021: Chaos synchronization in generalized Lorenz systems and an application to image encryption. *Commun. Nonlinear Sci. Numer. Simul.*, **96**, 105708, <https://doi.org/10.1016/j.cnsns.2021.105708>.
- Moore, E. H., 1920: On the reciprocal of the general algebraic matrix. *Bull. Amer. Math. Soc.*, **26**, 394–395.
- Orrell, D., L. Smith, J. Barkmeijer, and T. N. Palmer, 2001: Model error in weather forecasting. *Nonlinear Processes Geophys.*, **8**, 357–371, <https://doi.org/10.5194/npg-8-357-2001>.
- Osinga, H. M., 2018: Understanding the geometry of dynamics: The stable manifold of the Lorenz system. *J. Roy. Soc. N. Z.*, **48**, 203–214, <https://doi.org/10.1080/03036758.2018.1434802>.
- Park, J., S. Moon, J. M. Seo, and J.-J. Baik, 2021: Systematic comparison between the generalized Lorenz equations and DNS in the two-dimensional Rayleigh–Bénard convection. *Chaos*, **31**, 073119, <https://doi.org/10.1063/5.0051482>.
- Pecora, L. M., and T. L. Carroll, 1990: Synchronization in chaotic systems. *Phys. Rev. Lett.*, **64**, 821–824, <https://doi.org/10.1103/PhysRevLett.64.821>.

- Penrose, R., 1955: A generalized inverse for matrices. *Math. Proc. Cambridge Philos. Soc.*, **51**, 406–413, <https://doi.org/10.1017/S0305004100030401>.
- Privé, N. C., and R. M. Errico, 2013: The role of model and initial condition error in numerical weather forecasting investigated with an observing system simulation experiment. *Tellus*, **65A**, 21740, <https://doi.org/10.3402/tellusa.v65i0.21740>.
- Pu, Z., and J. Hacker, 2009: Ensemble-based Kalman filters in strongly nonlinear dynamics. *Adv. Atmos. Sci.*, **26**, 373–380, <https://doi.org/10.1007/s00376-009-0373-9>.
- Shen, B.-W., 2014: Nonlinear feedback in a five-dimensional Lorenz model. *J. Atmos. Sci.*, **71**, 1701–1723, <https://doi.org/10.1175/JAS-D-13-0223.1>.
- , 2015: Nonlinear feedback in a six-dimensional Lorenz model: Impact of an additional heating term. *Nonlinear Processes Geophys.*, **22**, 749–764, <https://doi.org/10.5194/npg-22-749-2015>.
- Shlyaeva, A., J. S. Whitaker, and C. Snyder, 2019: Model-space localization in serial ensemble filters. *J. Adv. Model. Earth Syst.*, **11**, 1627–1636, <https://doi.org/10.1029/2018MS001514>.
- Sparrow, C., 1982: *The Lorenz Equations: Bifurcations, Chaos, and Strange Attractors*. Springer-Verlag, 284 pp.
- Talagrand, O., and P. Courtier, 1987: Variational assimilation of meteorological observations with the adjoint vorticity equation. I: Theory. *Quart. J. Roy. Meteor. Soc.*, **113**, 1311–1328, <https://doi.org/10.1002/qj.49711347812>.
- Thépaut, J.-N., and P. Courtier, 1991: Four-dimensional variational data assimilation using the adjoint of a multilevel primitive-equation model. *Quart. J. Roy. Meteor. Soc.*, **117**, 1225–1254, <https://doi.org/10.1002/qj.49711750206>.
- Thompson, P. D., 1957: Uncertainty of initial state as a factor in the predictability of large scale atmospheric flow patterns. *Tellus*, **9**, 275–295, <https://doi.org/10.1111/j.2153-3490.1957.tb01885.x>.
- Tong, M., and M. Xue, 2005: Ensemble Kalman filter assimilation of Doppler radar data with a compressible nonhydrostatic model: OSS experiments. *Mon. Wea. Rev.*, **133**, 1789–1807, <https://doi.org/10.1175/MWR2898.1>.
- Tucker, W., 1999: The Lorenz attractor exists. *C. R. Acad. Sci., Ser. 1 Math.*, **328**, 1197–1202, [https://doi.org/10.1016/S0764-4442\(99\)80439-X](https://doi.org/10.1016/S0764-4442(99)80439-X).
- Van Leeuwen, P. J., 1999: Comments on “Data assimilation using an ensemble Kalman filter technique.” *Mon. Wea. Rev.*, **127**, 1374–1377, [https://doi.org/10.1175/1520-0493\(1999\)127<1374:CODAUA>2.0.CO;2](https://doi.org/10.1175/1520-0493(1999)127<1374:CODAUA>2.0.CO;2).
- Whitaker, J. S., and T. M. Hamill, 2002: Ensemble data assimilation without perturbed observations. *Mon. Wea. Rev.*, **130**, 1913–1924, [https://doi.org/10.1175/1520-0493\(2002\)130<1913:EDAWPO>2.0.CO;2](https://doi.org/10.1175/1520-0493(2002)130<1913:EDAWPO>2.0.CO;2).
- Yang, S.-C., and Coauthors, 2006: Data assimilation as synchronization of truth and model: Experiments with the three-variable Lorenz system. *J. Atmos. Sci.*, **63**, 2340–2354, <https://doi.org/10.1175/JAS3739.1>.
- , E. Kalnay, and B. Hunt, 2012: Handling nonlinearity in an ensemble Kalman filter: Experiments with the three-variable Lorenz model. *Mon. Wea. Rev.*, **140**, 2628–2646, <https://doi.org/10.1175/MWR-D-11-00313.1>.
- Yeong, H. C., R. T. Beeson, N. S. Namachchivaya, and N. Perkowski, 2020: Particle filters with nudging in multiscale chaotic systems: With application to the Lorenz'96 atmospheric model. *J. Nonlinear Sci.*, **30**, 1519–1552, <https://doi.org/10.1007/s00332-020-09616-x>.
- Yoden, S., 2007: Atmospheric predictability. *J. Meteor. Soc. Japan*, **85B**, 77–102, <https://doi.org/10.2151/jmsj.85B.77>.
- Zhang, Y., K. Ide, and E. Kalnay, 2015: Bred vectors of the Lorenz63 system. *Adv. Atmos. Sci.*, **32**, 1533–1538, <https://doi.org/10.1007/s00376-015-4275-8>.